Bi©hemistry

pubs.acs.org/biochemistry Article

Heme-Edge Residues Modulate Signal Transduction within a Bifunctional Homo-Dimeric Sensor Protein

Dayna C. Patterson, Yilin Liu, Sayan Das, Neela H. Yennawar, Jean-Paul Armache, James R. Kincaid,* and Emily E. Weinert*



Cite This: Biochemistry 2021, 60, 3801–3812



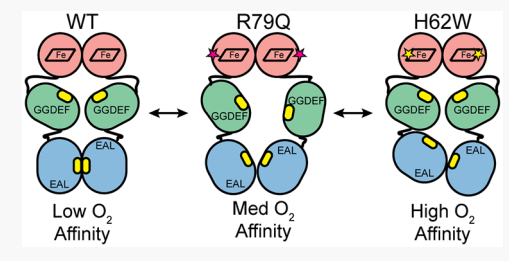
ACCESS

Metrics & More



SI Supporting Information

ABSTRACT: Bifunctional enzymes, which contain two domains with opposing enzymatic activities, are widely distributed in bacteria, but the regulatory mechanism(s) that prevent futile cycling are still poorly understood. The recently described bifunctional enzyme, DcpG, exhibits unusual heme properties and is surprisingly able to differentially regulate its two cyclic dimeric guanosine monophosphate (c-di-GMP) metabolic domains in response to heme gaseous ligands. Mutagenesis of heme-edge residues was used to probe the heme pocket and resulted in decreased O₂ dissociation kinetics, identifying roles for these residues in modulating DcpG gas sensing. In addition, the resonance Raman



spectra of the DcpG wild type and heme-edge mutants revealed that the mutations alter the heme electrostatic environment, vinyl group conformations, and spin state population. Using small-angle X-ray scattering and negative stain electron microscopy, the heme-edge mutations were demonstrated to cause changes to the protein conformation, which resulted in altered signaling transduction and enzyme kinetics. These findings provide insights into molecular interactions that regulate DcpG gas sensing as well as mechanisms that have evolved to control multidomain bacterial signaling proteins.

■ INTRODUCTION

Heme proteins serve a wide variety of roles in nature, ranging from oxygen transporters to catalysts to gas sensors. This functional diversity is made possible by the tuning of heme properties through heme pocket amino acid side chains that directly coordinate the heme iron or provide residues within proximity to the heme macrocycle. Residues near the heme can interact with its vinyl or propionate substituents, possibly inducing out of plane distortions. Variations in the heme pocket architecture, including resident water molecules, have yielded a diverse family of proteins with reduction potentials that span 1 V. Within the larger hemoprotein family, heme sensor proteins are used throughout the kingdoms of life to sense gaseous ligands, such as nitric oxide (NO), carbon monoxide (CO), and oxygen (O₂), and typically contain a proximal histidine ligand and, for O₂ binding proteins, have a distal pocket with hydrogen bonding residues.

Many organisms use heme-based sensor proteins to sense and respond to changes in their gaseous environment by binding diatomic ligands, such as NO, CO, and O₂, through the use of a variety of heme domains, including sensor globin, Per-Arnt-Sim (PAS), and Heme Nitric oxide-OXygen (H-NOX) domains. To date, heme sensor proteins have been demonstrated to respond to one primary ligand, with other diatomic ligands either not affecting their downstream protein/domain or having more modest effects than the physiological ligand. Si,16,18-20 In contrast, we recently characterized a globin coupled sensor (GCS) protein that is a bifunctional enzyme

from the bacterium Paenibacillus dendritiformis C454 (DcpG). GCS proteins consist of an N-terminal sensor globin domain linked by a middle domain of varying length to an output domain. In the case of DcpG, the protein contains both c-di-GMP synthesis (GGDEF) and hydrolysis (EAL) domains that are differentially regulated by O₂ and NO.²¹ C-di-GMP is a bacterial second messenger that regulates biofilm formation and is an important regulator of motility and virulence.²² For DcpG, NO binding activates c-di-GMP synthesis within the GGDEF domain relative to Fe^{II} unligated, while O₂ binding is inhibitory. In contrast, O2 binding results in activation of c-di-GMP hydrolysis by the EAL domain, relative to Fe^{II} unligated, while NO (and CO) have no significant effects. Using smallangle x-ray scattering (SAXS) and negative stain electron microscopy (EM), we demonstrated that DcpG in the Fe(II)-O2 ligation state forms a dimer that physically distances the GGDEF domains, inhibiting activity, while allowing formation of the active EAL domain dimer.²¹ In addition, DcpG was found to exhibit surprisingly rapid O2 and NO dissociation rates from the sensor globin domain and, using spectroelectrochemistry, the globin domain was demonstrated to have

Received: August 28, 2021
Revised: November 16, 2021
Published: November 29, 2021





two distinct high midpoint potentials (+418 and 279 mV vs the standard hydrogen electrode (SHE)), demonstrating the non-equivalency of the hemes within the DcpG homodimer.²¹

The atypical ligand dissociation rates and unique ability of DcpG to differentially control activity of the two enzymatic domains led us to probe here in this study the heme characteristics that allow the protein to respond differentially to two ligands. Using a combination of mutagenesis, enzyme kinetics, ligand binding kinetics, resonance Raman spectroscopy, and structural studies, we have identified roles for hemeedge amino acid residues in modulating DcpG heme conformation and enzyme activity. These results improve our understanding of the factors controlling heme electronics within heme proteins and provide new details regarding the sensor globin fold within GCS proteins.

EXPERIMENTAL SECTION

Protein Expression and Purification. The codonoptimized gene for DcpG (Uniprot ID: H3SIC7; codon optimization performed by GenScript) was cloned into pET-20b(+) using Ndel and Xhol restriction sites. The resulting plasmid was transformed into OverExpress C41(DE3) pLysS (Lucigen) via heat shock, and positive transformants were selected on LB medium containing ampicillin (DOT Scientific Inc.) (100 μ g mL⁻¹) and chloramphenicol (Research Products Int.) (30 μ g mL⁻¹). An approach known as the plating method was used obtain optimal protein expression.²³ Briefly, a single colony of pet20b(+)-DcpG plasmid-containing cells was suspended in 200 mL of autoclaved deionized water and vigorously shaken. The suspension was plated on LB medium containing ampicillin (100 µg mL⁻¹) and chloramphenicol (30 $\mu g \text{ mL}^{-1}$) and incubated at 37 °C. All colonies were scraped off and suspended in expression media (45 g of yeast extract (Research Products Int.), 1.6 g of KH₂PO₄ (Research Products Int.), 13.0 g of K₂HPO₄ (Research Products Int.), and 1% glycerol (Sigma Aldrich) per 1 L). The cells were grown at 37 $^{\circ}$ C, and aminolevulinic acid (Sigma Aldrich) (500 μ M final concentration) was added to the culture at $OD_{600} = 0.3$. The temperature was lowered to 18 $^{\circ}$ C, and the cells were grown to $OD_{600} = 0.7$. Cells were then induced with IPTG (Research Products Int.) (0.5 mM) and allowed to express the DcpG protein for 18-20 h prior to being harvested by centrifugation (4000g at 4 °C, 20 min), and the resulting cell pellet was frozen at -80 °C until use.

For purification, the cell pellet was thawed and suspended in Buffer A (50 mM Tris (Research Products Int.), 300 mM NaCl (Research Products Int.), 20 mM imidazole (Sigma Aldrich) (pH 7.5) with protease inhibitors (benzamidine HCl) (Research Products Int.), and Pefabloc SC (Sigma Aldrich)). The cells were lysed using a homogenizer (Avestin, Inc.), and the resulting lysate was centrifuged at 130,000g in a Beckman Optima L-90X ultracentrifuge at 4 °C for 1 h. All subsequent purification steps were performed at 4 °C. The supernatant was applied to a pre-equilibrated HisPur Ni-column (Fisher Scientific), and DcpG was eluted with Buffer B (50 mM Tris, 300 mM NaCl, and 250 mM imidazole, pH 7.5) at a flow rate of 1.0 mL/min. Purified DcpG was desalted eluting using a S200 gel filtration column (GE Healthcare) that had been equilibrated with Buffer C (50 mM Tris, 50 mM NaCl, 1 mM DTT (Research Product Int.), and 5% glycerol (v/v), pH 7.5) at a flow rate of 1.0 mL/min. Fractions containing DcpG were collected and concentrated via ultrafiltration (YM-10, 10 kDa MWCO filter, Millipore), aliquoted, flash frozen, and stored at -80 °C until use. Protein purity was assessed by sodium dodecyl sulfate-polyacrylamide gel electrophoresis (SDS-PAGE) (Figure S1A), and concentrations were determined using the Bradford Microassay (Bio-Rad Laboratories). DcpG variants (H62A, H62Y, H46F, H62W, R79A, and R79Q) were expressed and purified in an analogous manner to DcpG WT (Figure S1).

Site-Directed Mutagenesis. Variants of full-length DcpG were generated using the QuikChange protocol from Stratagene using materials from a Phusion High-Fidelity PCR Kit (Table S1). The mixture was run at the cycling parameters provided by the QuikChange protocol from Strategene using a BioRad C1000 Touch Thermal Cycler. Positive PCR were determined by gel electrophoresis and were transformed into DH5 alpha competent cells and plated on LB agar medium containing ampicillin (100 μ g mL⁻¹). Positive transformants were grown overnight in LB media containing ampicillin (100 μ g mL⁻¹). The DNA plasmid was extracted from overnight growth using a GenElute Plasmid miniprep kit. The accuracy of each substitution was verified by sequencing (Eurofins Genomics). The mutagenic primers used to create each variant are listed in Table S1.

Electronic Spectroscopy. UV-visible spectroscopy spectra were acquired from 800 to 200 nm using an Agilent Cary 100 spectrophotometer with an Agilent Technologies Cary Temperature Controller. The spectra were recorded in a 1 cm path length quartz cuvette. Preparation of complexes was carried out as previously described except that the proteins were prepared in Buffer C (Figure S2). ^{24,25} Briefly, DcpG is purified in the Fe(II)-O₂ ligation state. A 200 μ L aliquot of 80 μM DcpG is transferred into the anaerobic chamber where a solution of 500 µM sodium dithionite (Millipore Sigma) is prepared with anaerobic Buffer C. A 10 μ L aliquot of 500 μ M sodium dithionite is added to DcpG and left to sit for 30 min. The mixture was then desalted using a PD-10 column that was equilibrated with Buffer C and checked using the spectrophotometer for the fully reduced Fe(II) ligation state. For the Fe(II)-NO sample, 5 μL of 10 mM DEA-NONOate (Cayman Chemical) dissolved in anaerobic 0.1 M NaOH was added to the protein. The Fe(II) ligation states of the heme-edge variants were prepared analogous to DcpG WT (Figure S2).

O₂ Dissociation Rates. O₂ dissociation rates were performed as previously described with the following modifications. 20,24,26 DcpG and variants (3–5 μM) for O₂ dissociation rates and a 10 mM sodium dithionite trap were prepared in anaerobic Buffer C in an anaerobic chamber (Coy Labs). Saturating CO was not used as part of the trap. The dissociation of O₂ from the heme was monitored using an SX20 stopped flow equipped with a diode array detector and fit globally using Pro-KII (Applied Photophysics). Additional fitting analysis of raw data was performed using Igor Pro (Wavemetrics; Figure S3).

Resonance Raman Spectroscopy. Sample Preparation. To prepare the DcpG Fe(III) (wild type, H62A and R79A mutants), each sample (100 μ L of 100 μ M) was first buffer exchanged into 50 mM Hepes 50 mM KCl pH 7.5 buffer, and the protein was then oxidized by adding KFe(CN)₆ solution to a final concentration of 5 mM. The excess KFe(CN)₆ was removed from DcpG samples by passing through a PD10 desalting column (GE Healthcare). The protein was finally concentrated to 100 μ M for rR measurements. The deoxy samples were generated by evacuation of the oxygenated samples on a vacuum line and then refilling with argon.

Sufficient dithionite solution was added to fully reduce the samples, as monitored with a device capable of recording electronic absorption spectra from an NMR tube (model CHEM2000-VIS, Ocean Optics Inc., Dunedin, FL).

Resonance Raman Measurements. The ferric samples were measured with the 406.7 nm excitation line from a Kr+ laser (Coherent Innova Sabre Ion Laser), whereas the ferrous samples were acquired with the 441.6 nm line from a He-Cd laser (IK Series He–Cd laser, Kimmon Koha Co., Ltd.). All spectra were measured using a Spex 1269 spectrometer equipped with a Spec-10 LN liquid nitrogen-cooled detector (Princeton Instruments, NJ). The slit width was 150 μ m, and the laser power incident on all samples was ~10 mW; the spectra were calibrated with data acquired for fenchone and processed with Grams/32 AI software (Galactic Industries, Salem, NH).

Diguanylate Cyclase (DGC) Enzyme Kinetics. Prior to DGC kinetic assays, DcpG variants and EcDosP²⁷ were reduced and various DcpG complexes were formed as previously described. 24,25,27 The ligation/oxidation state of the heme was determined by UV-vis spectroscopy before each enzyme assay. All Fe(II), Fe(II)-NO, and Fe(II)-CO kinetics were measured in an anaerobic chamber (Coy Laboratories). The EnzChek pyrophosphate kit (Life Technologies) was used according to the manufacturer's instructions with the exception that DcpG and a phosphodiesterase (EcDosP) were added, and the reactions were initiated with varying concentrations of GTP (Sigma), as described for other GCS proteins. 20,28 The EnzChek kit monitors production of pyrophosphate from the enzymatic conversion of GTP to c-di-GMP. PPi is converted to Pi via an inorganic phosphatase and the resulting Pi is used by a nucleotide phosphorylase to enzymatically convert 2-amino-6-mercapto-7-methylpurine ribonucleoside (MESG) to ribose 1-phosphate and 2-amino-6-mercapto-7-methylpurine. The enzymatic conversion of MESG results in a shift in absorbance maximum from 330 to 360 nm. A360 readings were monitored every 30 s for 180 min.

Assays were performed in triplicate in 96-well plates containing four protein concentrations (0.25–2.5 μ M) and five GTP concentrations (0–1000 μ M). EcDosP was included at 3-molar excess to eliminate inhibition of cyclase activity by the produced c-di-GMP. Plates were monitored using an Epoch2 plate reader and Gen5 software (Biotek). The entire plate assay (including triplicates) was repeated at least twice with different protein preparations to account for day to day and protein batch variability. Subsequent analyses to determine enzymatic rates were performed using Igor Pro (Wavemetrics).

Phosphodiesterase (PDE) Enzyme Kinetics. Prior to PDE kinetic assays, the proteins were reduced, and various complexes were formed as previously described, 24,25 and the ligation/oxidation state of the heme was determined by UVvis spectroscopy. All Fe(II), Fe(II)-NO, and Fe(II)-CO kinetics were measured in an anaerobic chamber. The EnzChek phosphate kit (Life Technologies) was used according to the manufacturer's instructions with the exception that DcpG was added, and the reactions were initiated with varying concentrations of c-di-GMP. 5'-Nucleotidase from Crotalus atrox venom (Enzo Life Sciences) also was added to the kit at a concentration of 100 units/mL per well. 5'-Nucleotidase catalyzes the hydrolysis of pGpG to GpG and phosphate but does not hydrolyze c-di-GMP.²¹ A360 readings were monitored every 30 s for 180 min. 21 A360 readings were monitored every 30 s for 180 min.

Assays were performed in triplicate in 96-well plates containing four protein concentrations (1.25–10 μ M) and five c-di-GMP (Axxora) concentrations (0–75 μ M). The entire plate assay (including triplicates) was repeated at least twice to account for day to day and protein batch variability. Subsequent analyses to determine enzymatic rates were performed using Igor Pro (Wavemetrics).

Small-Angle X-ray Scattering (SAXS). DcpG H62W, H62A, and R79Q protein samples at concentrations of 0.25, 0.50, 0.75, and 1.0 mg/mL were prepared in a buffer containing 50 mM Tris, 50 mM NaCl, and 5% glycerol (pH 7.5). All samples were centrifuged at 14,000 rpm for 20 min to minimize aggregation and to remove dust particles prior to analysis. DLS measurements were performed on the samples to ensure homogeneity (Table S2). Synchrotron SAXS data were collected at the macromolecular Cornell High Energy Synchrotron Source, MacCHESS, on the G1 beamline station. Data were collected at 293 K using a dual PILATUS 100K-S SAXS/WAXS detector and a wavelength of 1.264 Å. A 1.5 mm OD quartz glass capillary with 10 µm-thick walls in vacuo was used, and 30 μ L of the sample was loaded with a Hudson SOLO single-channel pipetting robot (Hudson Robotics Inc. Springfield, New Jersey). To reduce radiation damage, sample plugs were oscillated in the X-ray beam using a computercontrolled syringe pump. The sample capillary-to-detector distance was 1508.0 mm and allowed for simultaneous collection of small- and wide-angle scattering data, covering a broad momentum-transfer range (q range) of $0.0075-0.8 \text{ Å}^{-1}$ $(q = 4\pi \sin(\theta)/\lambda)$, where 2θ is the scattering angle). The energy of the X-ray beam was 9.808 keV, with a flux of 3×10^{11} photons/s and a diameter of 250 μ m \times 250 μ m. The synchrotron storage ring was running at 50 milliamps positron current. Exposure times of 10 s in 10 1 s frames were used for the measurements; this allowed monitoring for any radiation damage effect. No radiation damage was detected, and the 10 frames were averaged. The RAW software was used for initial data reduction and background buffer data subtraction.²⁹ The data at high concentrations showed no concentration dependence and was used for further analysis. The forward scattering I(0) and the radius of gyration (R_{σ}) were calculated using the Guinier approximation, which assumes that at very small angles $(q < 1.3/R_o)$, the intensity is approximated as I(q) = $I(0)\exp[-(qR_{\varphi})23]$. The molecular mass was estimated using a comparison with glucose isomerase and lysozyme standard protein data and Guinier fit and Kratky plots generated in the BioXTAS RAW software. For all further data analysis, the SAXS software suite ATSAS³⁰ was used. GNOM³¹ was used to calculate the pair-distance distribution function P(r), from which the maximum particle dimension (D_{max}) and R_{g} were determined (Table S3). Ab initio low-resolution solution models were reconstructed using DAMMIN³² for data in the range $(0.009 < q < 0.275 \text{ Å}^{-1})$. Ten models were generated from each program and averaged using DAMAVER.³³ The normalized spatial discrepancy parameter (NSD) obtained from DAMAVER indicated the similarity between models used for average calculations. NSD values ≤1.0 were obtained as expected for similar models. The theoretical scattering profiles of the constructed models were calculated and fitted to experimental scattering data using $CRYSOL^{34}$ (Figure S6).

Individual domains of the DcpG structures, globin, GGDEF, and EAL were generated using homology modeling in iTasser.³⁵ Possible tertiary and quaternary structures of globin-globin, EAL-GGDEF, GGDEF-GGDEF, and EAL-

EAL dimers were also modeled in iTasser and the PyMOL graphics software³⁶ using the corresponding sub-sequences and available high-resolution protein structures. The linker residues connecting the globin and GGDEF domains were allowed to have random-coil conformations. The various domain models were manually rotated and translated to fit into the SAXS solution envelope using PyMOL. The constraints used for building the DcpG dimer included keeping the established globin dimer intact and using the cross-linking data information for the wild type and mutants for positioning the other domains. The complete DcpG dimer model hence built was energy minimized using the Chimera³⁷ software. To evaluate the conformational flexibility of the domains in the manually fit dimer, SREFLEX³⁸ software was used with the domains and their individual dimers refined as independent rigid bodies. This ATSAS program uses normal mode analysis to estimate the flexibility of high-resolution models and improves their agreement with experimental SAXS data. In these refinement steps, the EAL and GGDEF domains were free to adopt different conformations relative to a fixed globin dimer.

Gradient Fixation (GraFix)^{39,40} Preparation of the Complexes. The purified sample was dialyzed into Buffer A (Buffer A: 20 mM HEPES-KOH pH 7.55, 60 mM KCl, 5% glycerol, 1.5 mM DTT, 2 mM MgCl₂) for 3 h in 4 °C. Buffer B and buffer C (Buffer B: 20 mM HEPES-KOH pH 7.55, 60 mM KCl, 10% glycerol, 1 mM DTT, and 2 mM MgCl₂; Buffer C: 20 mM HEPES pH 7.55, 60 mM KCl, 30% glycerol, 1 mM DTT, 2 mM MgCl₂, and 0.1% glutaraldehyde) were mixed using a gradient maker (Gradient Master, Biocomp). The prepared sample was then added on the top layer of the tube mixture and centrifuged overnight (Beckman Coulter Optima XL-100K). The solution in the tube was then fractionated and analyzed.

Electron Microscopy Sample Preparation and Data Collection. Continuous carbon grids were glow-discharged for 30 s using a Pelco easiGlow Cleaning System. We then deposited 3 μ L of purified sample, incubated it for 30 s on the grid at room temperature, negatively stained with five drops of 2% uranyl formate solution, and blotted dry. The grids were imaged using a Tecnai G^2 20 X-TWIN electron microscope equipped with a LaB6 source, operating at 200 keV at a nominal magnification of 17,500× (6.07 Å/pixel at the detector level).

The images were recorded on a Gatan US1000XP Ultrascan CCD camera (2048 × 2048, 14 μ m physical pixel size, Figure S8) at a defocus range of -1.5 to -3μ m and an electron dose of 25 e⁻/Å².

Image Processing. The collected images were contrast-inverted using EMAN2⁴¹ and imported into cryoSPARC v2.15⁴² for all subsequent data processing. After CTF calculations, 1500 particles were picked manually, classified in 2D, and used as templates for automated particle picking. After picking, 2D classification was used to eliminate "bad particles", and the selection was used for *ab initio* and subsequently homogeneous refinement. We also used 3D classification to further homogenize the sample in silico.

■ RESULTS AND DISCUSSION

Heme-Edge Residues Modulate O_2 Dissociation Kinetics. Most GCS proteins and sensor globins characterized to date exhibit slow, biphasic O_2 dissociation kinetics (Table 1); however, the GCS from *Bacillus subtilis* HemAT-*Bs* exhibits

Table 1. O_2 Dissociation of DcpG and Heme-Edge Variants^a

protein	$k_1 (s^{-1})$	$k_2 (s^{-1})$	$\% k_1$	% k ₂	ref
DcpG	12.07	87.30	18	82	21
DcpG H62A	2.11	12.38	52	48	TW
DcpG H62Y	2.61	22.00	30	70	TW
DcpG H62W	1.86	5.17	45	55	TW
DcpG H62F	0.70	2.09	54	46	TW
DcpG R79A	5.02	92.20	20	80	TW
DcpG R79Q	12.10	69.60	15	85	TW
PccGCS	0.56	3.87	56	44	20
BpeGreg	0.82	6.30	39	61	20
<i>Ec</i> DosC	13				11
HemAt-Bs	87	1900	NR	NR	43

^aTW: this work, NR: not reported. Standard deviations for rates and rate percentages are less than 5% of the measured value.

 O_2 dissociation rates even faster than DcpG.⁴³ Therefore, to identify key differences that result in rapid O_2 dissociation rates, the heme pocket of DcpG was further considered using a homology model of the globin domain (Figure 1; the model generated using Phyre2⁴⁴). A histidine (H) at the DcpG heme edge (position 62) was identified and, based on the globin domain sequence alignment (Figure 1B, arrow c), found to be conserved in HemAt-Bs, but not the other GCS proteins, which have tryptophan (W) at this position. As it previously has been shown that heme-edge residues that π -stack to the heme can control ligand affinity and midpoint potential, 20,45,46 we hypothesized that DcpG H62 influences the O_2 dissociation rates by modulating heme electronics.

Site-directed mutagenesis was used to generate the H62A, H62W, H62Y, and H62F variants to determine the effect of changing electronics and hydrogen bonding at the heme edge on the O₂ dissociation rates. Each of the H62 variants resulted in decreased k_1 and k_2 rates (Table 1), with rates for the H62W variant being nearly the same as those of PccGCS and BpeGReg, which contain heme-edge tryptophan residues. 20,47 In addition, the percentages of k_1 and k_2 for the H62 variants are altered compared to the DcpG wild type, indicating that there may be differences in heme pocket conformation and/or side chain interactions between the variants and wild-type protein. Interactions between positively charged heme-edge His/Arg residues and the porphyrin ring in DcpG and HemAT-Bs could withdraw electron density from the heme, resulting in weaker Fe-O2 interactions and the observed rapid O₂ dissociation rates.

Heme-Edge Residues Affect Ligand-Dependent Signaling. To probe the effects of heme-edge residues on the signaling mechanism of DcpG ligand regulated activity, we investigated the effect of the H62W and R79Q heme-edge mutations on diguanylate cyclase (DGC) and phosphodiesterase (PDE) activity to determine if the heme edge is involved in signal transduction (Table 2 and Figure S4). For the DGC activity, both the H62W and R79Q variants exhibited the same trend as DcpG ($k_{\rm cat}$ Fe(II) > $k_{\rm cat}$ Fe(II)-O₂) as shown in Table 3; however, $k_{\rm cat}$ and $K_{\rm M}$ values for the mutants were substantially changed. The R79Q mutant, which is farther from the heme edge, exhibited ~2-fold and ~4-fold decreases in catalytic activity for the Fe(II) and Fe(II)-O₂ ligation states, respectively. The H62W variant exhibited the same ~2-fold decreased activity for the Fe(II) state but displayed a 9-fold decrease in activity for the Fe(II)-O₂ ligation state, as

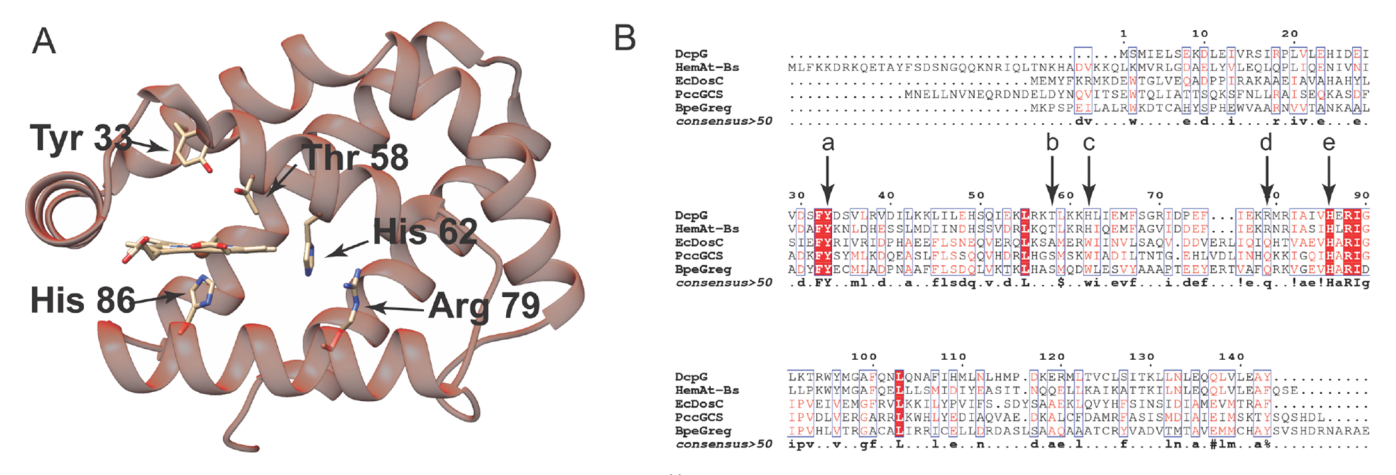


Figure 1. Homology model of DcpG and globin sequence alignment.⁴⁴ (A) Heme proximal, distal, and edge residues within the heme pocket are labeled. (B) Sequence alignment of sensor globin domains. (a) distal tyrosine (Y33); (b) secondary hydrogen bond donor threonine (T58); (c) heme-edge His/Trp (H62); (d) heme-edge Arg/Gln (R79); and (e) proximal histidine (H86). Numbering corresponds to DcpG.

Table 2. Kinetic Parameters for DcpG Heme-Edge Mutants' Ligand-Dependent DGC Activity at 25 $^{\circ}$ C (Mean \pm SD for Three Independent Experiments)

protein	ligation state	$k_{\rm cat~GTP}~({\rm min}^{-1})$	$K_{ m m~GTP}~(\mu m M)$
DcpG WT ²¹	Fe(II)	1.21 ± 0.07	284.4 ± 123.3
	Fe(II)-O ₂	0.45 ± 0.04	80.9 ± 33.5
DcpG H62W	Fe(II)	0.71 ± 0.03	77.9 ± 54.7
	Fe(II)-O ₂	0.05 ± 0.02	7.01 ± 3.71
DcpG R79Q	Fe(II)	0.69 ± 0.01	137.7 ± 23.6
	$Fe(II)-O_2$	0.22 ± 0.10	21.0 ± 7.5

Table 3. Kinetic Parameters for DcpG Heme-Edge Mutants' Ligand-Dependent PDE Activity at 25 $^{\circ}$ C (Mean \pm SD for Three Independent Experiments)

protein	ligation state	$k_{\rm cat\ c\text{-}di\text{-}GMP}\ ({\rm min}^{-1})$	$K_{\text{m c-di-GMP}} (\mu M)$
DcpG WT ²¹	Fe(II)	0.22 ± 0.01	8.35 ± 4.78
	Fe(II)-O ₂	0.54 ± 0.08	11.94 ± 4.65
DcpG H62W	Fe(II)	0.10 ± 0.01	6.4 ± 3.4
	Fe(II)-O ₂	0.25 ± 0.04	10.0 ± 4.3
DcpG R79Q	Fe(II)	no activity	
	Fe(II)-O ₂	0.14 ± 0.05	8.5 ± 3.1

compared to DcpG WT, indicating that the H62W variant has a greater effect on signal transduction than the R79Q variant. These data demonstrate that DcpG requires contacts between heme-edge residues and the porphyrin for full DGC activity. Furthermore, the heme-edge variants both exhibited decreased $K_{\rm M}$ values relative to DcpG (Table 2), suggesting that the mutations caused rearrangements in both the GTP binding site and the interface between the DGC domains that contains the GGDEF active site. However, the changes in $K_{\rm M}$ are unlikely to affect activity *in vivo* because GTP concentrations in log-phase bacteria are typically in the millimolar range. ⁴⁸

Although no other EAL-containing GCS proteins have been characterized to allow for comparison of the effect of DcpG heme mutations with another GCS, the H62W and R79Q variants can give insights into how these heme-edge residues affect PDE activity. The H62W and R79Q mutants exhibited the same trend as DcpG (Table 3) ($k_{\rm cat}$ Fe(II)-O₂ > Fe(II)); the H62W mutant resulted in a 2-fold decrease in the $k_{\rm cat}$ for each ligation state; however, the R79Q Fe(II) unligated variant exhibits no PDE activity, indicating that the R79Q mutation

disrupts PDE activity when in the Fe(II) state, but a signal can still be transduced when O_2 is bound (Table 3). The K_M for the heme-edge variants remains relatively unchanged, indicating that these mutations do not cause a major change to the c-di-GMP binding site in the EAL domain (Table 3).

Resonance Raman of the DcpG WT and Heme-Edge **Variants.** To provide further insights into the heme properties and interactions that weaken O2 affinity, resonance Raman experiments were performed on DcpG, DcpG H62A, and DcpG R79A Fe(III) and Fe(II) samples. Resonance Raman (rR) has been proven to be a powerful tool to detect subtle changes in the active sites of heme-based sensor proteins, allowing for additional information regarding the DcpG heme pocket. 49-54 Factors known to affect electronics of heme proteins include the electrostatic environment, 55,56 heme outof-plane distortion, 2,57,58 steric and electrostatic interactions of heme pocket amino acid residues with the vinyl and propionate peripheral substituents, $^{59-62}$ and solvent exposure of the heme.⁷ In the present case, the positively charged heme-edge residues in DcpG (protonated H62 and R79) could withdraw electron density from the heme, thereby decreasing O₂ affinity. In addition, it is possible that the heme could be less solventexposed within DcpG, as the protein structure has not yet been solved.

The resonance Raman spectra of DcpG, DcpG H62A, and DcpG R79A Fe(III) species are shown in Figure 2A-C. The heme macrocycle modes in the high frequency region are sensitive to the heme oxidation and spin state changes. In the wild-type DcpG (Figure 2A), the oxidation state marker, the ν_4 mode, appears at 1369 cm⁻¹, indicating the presence of a pure ferric species, while the spin state markers, the ν_3 and ν_2 modes, are observed at 1492 and 1568 cm⁻¹, respectively, confirming the presence of a five-coordinate high-spin (5cHS) heme. It is noted that a relatively strong $\nu(C=C)$ vinyl stretching mode is observed at 1634 cm⁻¹. In the low frequency region, the assigned heme skeletal modes in the wild-type protein are ν_7 (673 cm⁻¹), ν_8 (349 cm⁻¹), and ν_{15} (746 cm⁻¹). The band observed at 372 cm⁻¹ is attributed to the heme propionate bending coordinates, while those appearing at 411 and 430 cm⁻¹ are typically assigned to "vinyl bending" modes. The only significantly enhanced out-ofplane modes are γ_{21} and γ_{22} , both of E_g symmetry.^{49–54,57,63}

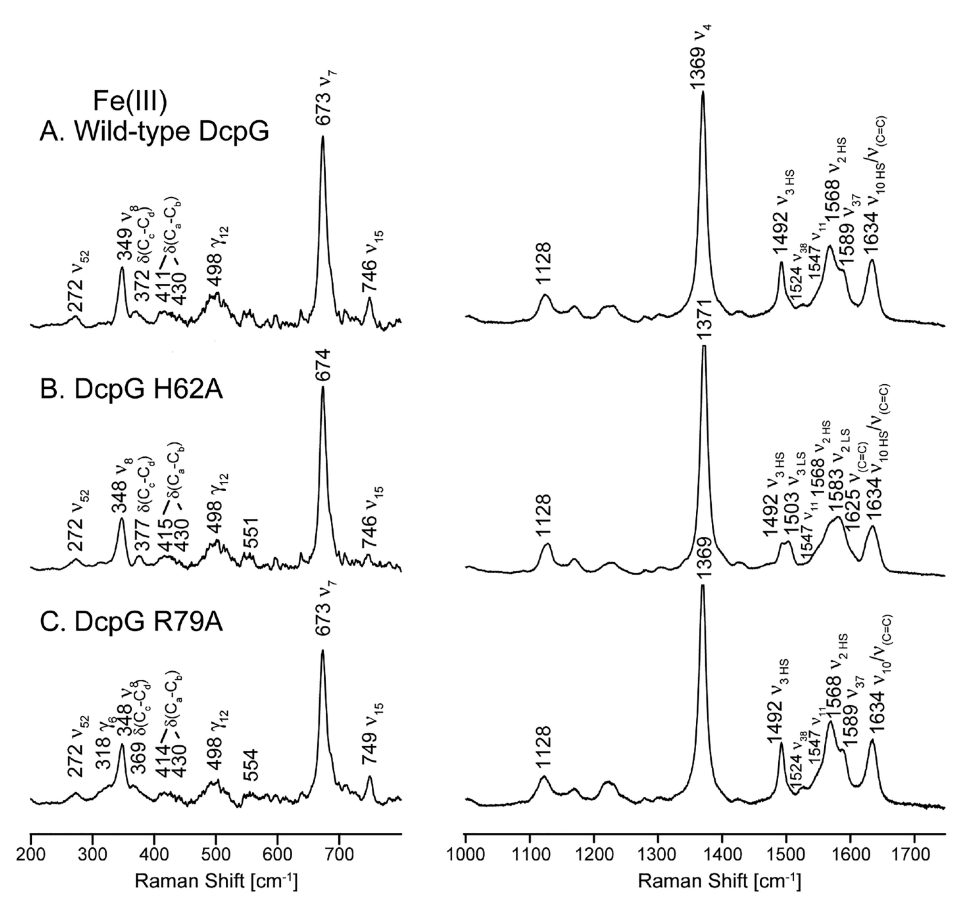


Figure 2. rR spectra of ferric DcpG in low (left panel) and high frequency (right panel) regions. (A) WT, (B) DcpG H62A, and (C) DcpG R79A in the high frequency regions.

Figure 2B (right panel) shows the high-frequency region of the H62A mutant, showing features characteristic of the ferric state, with the ν_4 oxidation state marker occurring at 1371 cm⁻¹. Interestingly, the ν_3 spin state marker bands are indicative of the presence of a mixture of five-coordinate high-spin (1492 cm⁻¹) and six-coordinate low-spin (1503 cm⁻¹) species; consistent with this, the ν_2 (spin-state marker) modes for five-coordinate high-spin (1568 cm⁻¹) and sixcoordinate low-spin (1583 cm⁻¹) are observed in the expected region. 49,51-54,63 At this point, it is not clear if the individual hemes in the DcpG H62A dimer are inequivalent upon oxidation, with one being five-coordinate high-spin and the other six-coordinate low-spin; alternatively, each heme of the dimer may be partially converted to the 6cLS state. Clearly, replacing the bulky His62 with Ala might alter the heme active site structure in several ways that influence the heme electronics. One major difference in the rR spectrum acquired for the H62A mutant is the appearance of a second vinyl $\nu(C=C)$ mode at 1625 cm⁻¹, this lower frequency mode being associated with a vinyl group adopting a more in-plane orientation with the pyrrole ring of the macrocycle; 64-66 significantly, it is noted that this orientation of the electronwithdrawing vinyl substituent can be expected to lead to some increase in the heme reduction potential.⁶¹ The most notable change in the low frequency region is the shift of the propionate bending mode from 372 to 377 cm⁻¹ for the H62A variant, such a shift typically reflecting increased H-bonding interactions with amino acid side chains, 59-62,67,68 though the magnitude of the expected effects on heme electronics remains unclear. $^{59-62,69}$

The rR spectrum of the R79A mutant (Figure 2C) exhibits a spectral pattern quite similar to that of the wild-type protein, showing a five-coordinate high-spin ferric heme, with the spin state markers observed at 1492 (ν_3) and 1568 (ν_2) and a vinyl C=C stretching mode coincident with that of the WT protein. The low-frequency region of ferric DcpG R79A mutant exhibits the propionate bending mode at 369 cm⁻¹, 3 cm⁻¹ lower than the wild type, indicative of a more disrupted H-bonding between propionate and nearby amino acid residues. Additionally, it is noted that an A_{2u} "pyrrole tilt" heme out-of-plane mode, γ_7 , occurring at 318 cm⁻¹, is weakly activated after mutating R79 to alanine.

In summary of the rR data acquired for the ferric forms of DcpG, the mutations of these two heme-edge residues have minimal effects on the planarity of the heme macrocycle, based on the lack of significant changes in the observed low frequency out-of-plane modes. On the other hand, replacement of the bulky H62 residue with Ala leads to heme pocket rearrangements, causing one of the heme vinyl groups to adopt a more planar alignment with the macrocycle pyrrole group, a reorientation that provides an understanding for the modest decrease in $\rm O_2$ dissociation rates of the variant. $\rm ^{59-61,70,71}$

Turning attention to the resonance Raman data for the ferrous forms of DcpG, DcpG H62A, and DcpG R79A, the spectra for the high frequency region are shown in Figure 3A–C (right panels). WT DcpG exhibits a ν_4 mode at 1354 cm⁻¹, which indicates the presence of a pure ferrous species while the

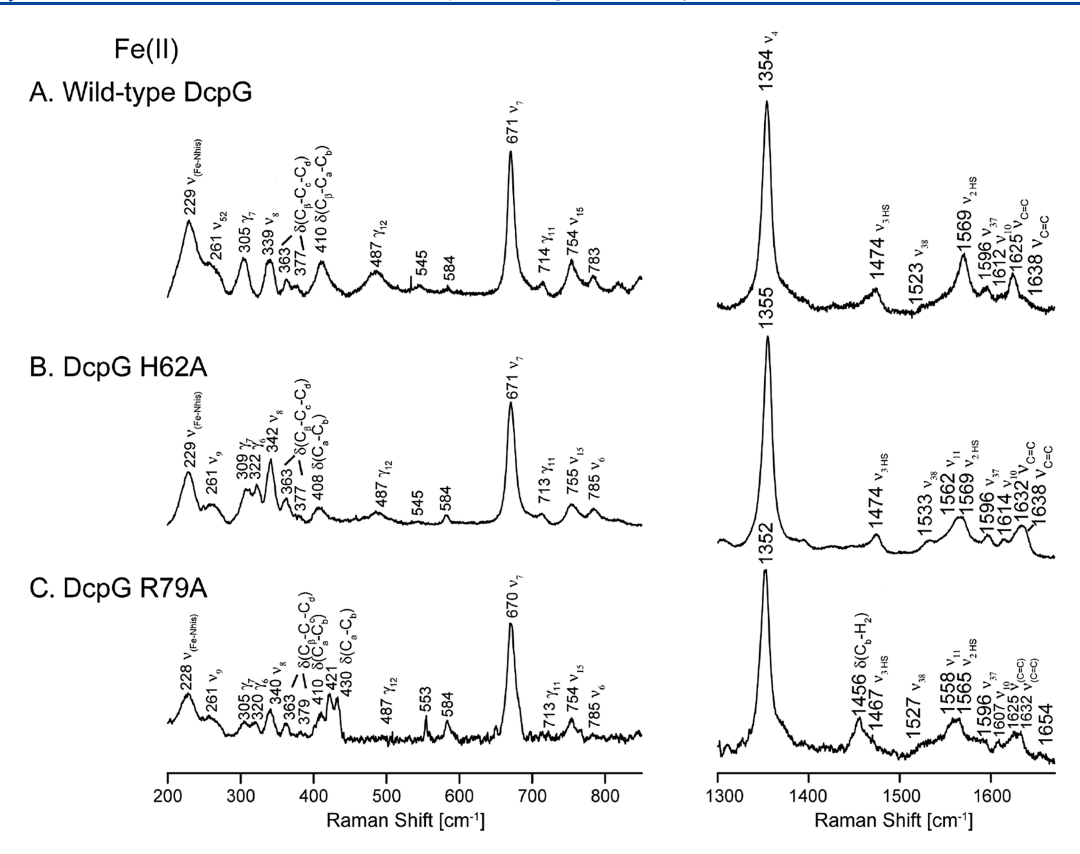


Figure 3. rR spectra of ferrous DcpG in low (left panel) and high frequency (right panel) regions. (A) WT, (B) DcpG H62A, and (C) DcpG R79A in the high frequency regions.

spin state markers, ν_3 , ν_2 , and ν_{10} , occurring at 1474,1569, and 1612 cm⁻¹, respectively, indicate a 5cHS species. Similarly, both H62A (Figure 3B) and R79A (Figure 3C) variants also exhibit features of a ferrous, five-coordinate high-spin species. 65,72 As was the case with the ferric species, the most interesting changes for the mutants involve the behavior of the vinyl groups. The WT protein exhibits a relatively intense vinyl C=C stretching mode at 1625 cm⁻¹, indicating a nearly planar orientation relative to the pyrrole rings, implying enhanced conjugation, along with a weak 1638 cm⁻¹ mode attributable to a small fraction of vinyl groups with an out-of-plane configuration. As is clarified in Figure S5, the expanded rR spectrum of the H62A is best fit with only a minor contribution of the (1625 cm⁻¹) in-plane vinyl group orientation, seemingly reflecting loss of the bulky His residue, and two features (1632 and 1638 cm⁻¹) ascribable to out-ofplane vinyl groups. The R79A variant, retaining the bulky H62 side chain, exhibits a relatively intense 1625 cm⁻¹ feature, along with a significant contribution (1632 cm⁻¹) from out-ofplane vinyl groups. One notable difference in the rR spectrum of this variant is the presence of a relatively strong new feature observed at 1456 cm⁻¹ that is most reasonably ascribed to a vinyl $\delta(CH_2)$ bending (scissoring) mode. 73 Consistent with this, reference to the low frequency spectra displayed in the left panel shows that the R79A variant does indeed exhibit new, relatively intense, vinyl $\delta(C_{\beta}-C_a-C_b)$ bending modes at 421 and 430 cm⁻¹ that are attributable to out-of-plane vinyl groups. 59,64,65

The most interesting finding in the low frequency region is the positioning of the proximal Fe- N_{his} stretching mode at 229 cm⁻¹, which is also present in both heme-edge mutants, indicating that mutating these heme-edge residues do not have

a significant impact on the proximal pocket. It is important to point out that the frequency of $\nu(\text{Fe-N}_{\text{his}})$ of DcpG is somewhat higher than seen in many other heme-based sensor proteins, which typically exhibit low Fe-N_{his} stretching modes occurring between 204 and ~225 cm⁻¹.^{74,75} Generally, such increases in the $\nu(\text{Fe-N}_{\text{his}})$ stretching modes are attributable to the presence of proximal pocket H-bond acceptor groups that increase the basicity of the proximal histidine. The indeed, such increases of the Fe-His bond strength may account for the rapid dissociation of O₂ and NO.

Several other features in the low frequency region are worth noting. First, several sensitive to out-of-plane heme distortion are activated or change intensity upon mutation, (e.g., γ_6 , γ_7 , and γ_{21}). As reported earlier by Shelnutt's group, various heme deformation types were cataloged based on various heme proteins using their NSD (normal-coordinate structure decomposition) analysis. 57,80,81 The appearance of relatively strong heme out-of-plane modes of A_{211} symmetry, γ_6 and γ_7 , are consistent with an out-of-plane (doming) distortion of the heme, as is typical of deoxy globins. It is also noted that the intensity of E_{σ} symmetry out-of-plane mode, γ_{21} , is enhanced in both H62A and R79A mutants, indicating the presence of a waving distortion of the heme. This double degenerate normal mode occurs at a relative higher frequency, thus requiring a greater external perturbation upon the heme macrocycle. The observation of these three enhanced modes of A_{2u} and E_g symmetry in both mutants is clearly indicative of non-planar deformations of the heme, which is expected to result in distinct alterations of the chemical and physical properties of the enzyme.⁸¹ Additionally, the H62A and R79A mutations cause an increase in the relative intensity of the 363 cm⁻¹ bending mode of the propionate group, indicating a structural

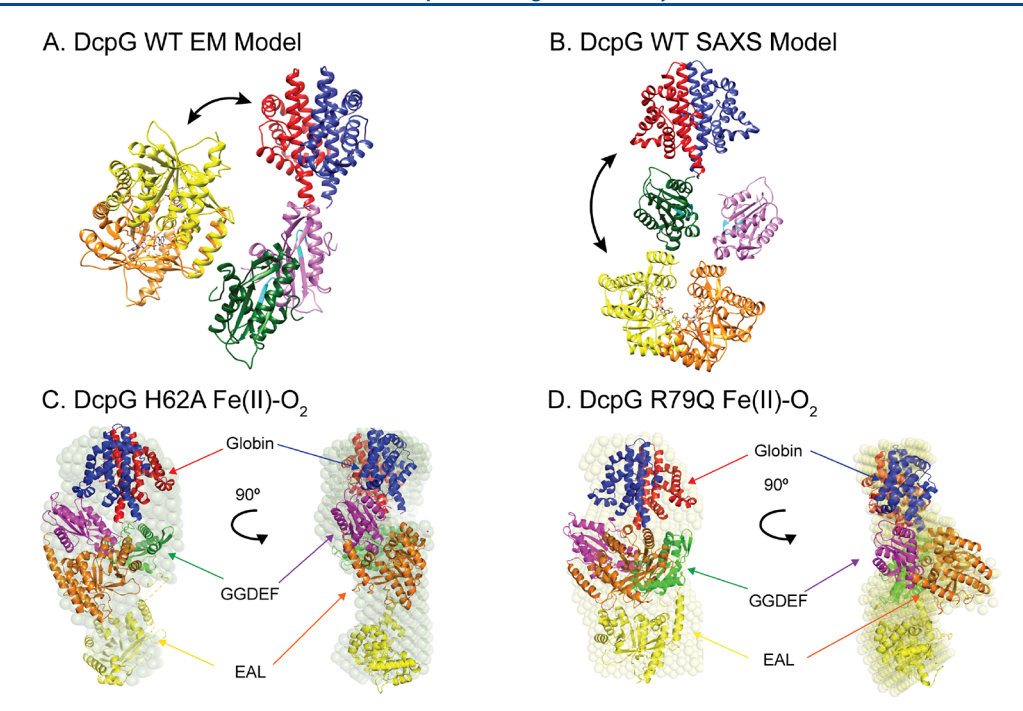


Figure 4. Heme-edge mutations cause domain reorientation. DcpG WT model from negative stain (A) EM and (B) SAXS.²¹ The models suggest flexibility that allows the EAL domains to move toward and away from the globin domains. Domain colors are the same as in (C, D), with the GGDEF active site motif highlighted in cyan. (C) The SAXS envelope shows that the globin domains of DcpG H62A form a tight dimer (blue and red), with the GGDEF and EAL domains in an extended conformation in one monomer (shown in green and yellow, respectively). In the second monomer the GGDEF and EAL domains form a tight heterodimer (shown in magenta and orange, respectively). (D) Based on the SAXS envelope, the globin domains of DcpG R79Q form a tight dimer (blue and red), with the cyclase and phosphodiesterase domains in an extended conformation in one monomer (shown in green and yellow, respectively). In the second monomer, the cyclase and phosphodiesterase domains form a tight heterodimer (shown in magenta and orange, respectively). The SAXS-derived domain organization of the H62W mutant after Sreflex is similar to that seen for the R79Q mutant. The extended monomer (red-green-yellow) shows a large interdomain re-organization compared to the H62A mutant.

reorientation and disrupted hydrogen bonding between propionate groups and surrounding amino acid residues. These data further support our hypothesis that structural rearrangements within the heme pocket result in differences in ligand-dependent activity between the variants.

SAXS and Negative Stain EM Analyses of DcpG Heme-Edge Variants. To gain insights into the conformational changes that could be linked to the mutations, SAXS and negative stain EM were used to probe the heme-edge variants and compared to WT models (Figure 4A,B).²¹ The DcpG WT was found to form a tight globin dimer with EAL active sites dimerized for high activity. However, the GGDEF active sites are not in close proximity, likely resulting in the observed low DGC activity in the Fe(II)-O₂ state.²¹ The DcpG H62A SAXS model found that the globin domains form a tight dimer; however, the DGC and PDE domains are not associated in one monomer, and the linker between the globin and GGDEF domains is modeled in an extended conformation (Figure 4C and Figure S7). In the second monomer, the DGC and PDE domains form a tightly coupled structure interacting with the globin domain and superposition shows that the domain organization of the folded monomer is similar to that seen in

The SAXS models of DcpG H62W and R79Q also show the globin domains in a tight dimer, similar to the H62A mutant, with the GGDEF and EAL domains in an extended conformation in one monomer (Figure 4D). In the second monomer, the quaternary structure is more folded with the DGC and PDE domains closely interacting and facing their

active sites toward each other. The organization of the H62W mutant is very similar to that seen for the R79Q mutant. Superposition of the H62W/R79Q and H62A SAXS derived structures shows that the extended monomer of H62W exhibits interdomain rotation due to the flexible linker and the folded monomers of H62W/R79Q have the globin and GGDEF-EAL coupled unit oriented differently than in H62A (Figure S7).

To investigate the differences between the variants, we carried out negative stain EM studies on the proteins to obtain greater structural detail (Figure 5 and Figure S8). We created individual 3D reconstruction EM maps of both heme-edge mutants from the single particle analysis of homogenously dispersed protein particles (Figure S8). Surprisingly, DcpG H62W produced two EM maps, indicating that this heme-edge mutant has multiple conformations, class 1 and class 2 (Figure 5A,B), potentially due to increased flexibility between the domain-domain interactions. DcpG R79Q only produced one EM map (Figure 5C), indicating that this conformation is more stable and lacks the flexibility compared to DcpG H62W. Interestingly, the DcpG R79Q EM map has a more detailed envelope than both DcpG H62W maps. The R79Q construct also has a lower Porod volume as seen by SAXS analysis compared to the H62W variant (Table S3). Therefore, this heme-edge mutant could provide a promising route toward a higher-resolution structure using cryo-EM due to its stability and negative stain characteristics.

The conformational differences between DcpG H62W and DcpG R79Q as well as the greater flexibility of H62W likely are

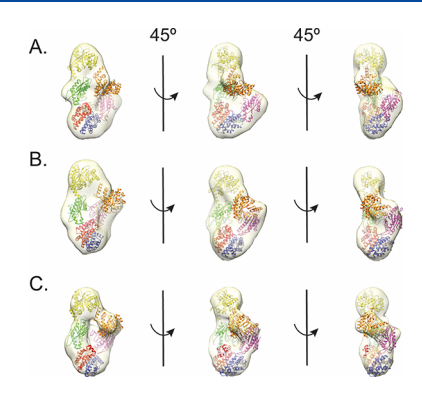


Figure 5. Comparison of DcpG H62W and DcpG R79Q models. The first monomer domains of the dimer are highlighted as follows: globin (red), GGDEF (green), and EAL (yellow). The second monomer domains of the dimer are highlighted as follows: globin (blue), GGDEF (magenta), and EAL (yellow). (A) DcpG H62W class 1 domain models fitted into its EM map (A). (B) DcpG H62W class 2 domain model fitted into its EM map. (C) DcpG R79Q domain model fitted into its EM map.

correlated with the changes in enzymatic activity. The two DGC domains are closer together in the R79Q protein, which would allow the dimeric active site to form more readily and result in the greater DGC activity. In contrast, conformation 1 (Figure 5A) of H62W appears to position the EAL domains in proximity; although the active site resides within a single protein, EAL domains typically exhibit greater PDE activity as dimers. Therefore, H62W has a higher PDE activity. However, higher resolution data is needed to provide exact details of the conformations and its effect on the DGC and PDE enzyme activities.

CONCLUSIONS

In conclusion, our work provides information about how heme-edge residues can modulate the heme properties of an unusual dual ligand-sensing heme protein, DcpG, that exhibits rapid O2 and NO dissociation rates, and differential activation of enzymatic domains, and heme-edge residues that can modulate these characteristics. A histidine residue at the heme edge modulates O2 dissociation rates, with mutation to tryptophan or phenylalanine, resulting in slower dissociation kinetics. Interactions between the histidine and heme may affect heme electronics, resulting in the rapid ligand dissociation rates observed for DcpG and HemAT-Bs. 43 Mutation of the heme-edge residues resulted in conformational rearrangements of the heme, particularly of the vinyl groups and propionates, suggesting that the histidine and arginine residues may be required for proper ligand-dependent signaling. This work extends our understanding of the factors controlling heme properties and provides new links between heme-edge residues, heme conformation, and ligand-dependent signaling.

ASSOCIATED CONTENT

Supporting Information

The Supporting Information is available free of charge at https://pubs.acs.org/doi/10.1021/acs.biochem.1c00581.

SDS-PAGE analysis results, UV-visible spectra, stopped flow kinetics, representative Michaelis—Menten kinetics, deconvoluted rR spectra, SAXS scattering profiles, Kratky plots, and ATSAS-Crysol program overlay,

SAXS-derived solution-based bead model, representative negative stain EM images and 2D class averages, primers used, DLS results, and SAXS structural parameters (PDF)

AUTHOR INFORMATION

Corresponding Authors

James R. Kincaid — Department of Chemistry, Marquette University, Milwaukee, Wisconsin 53233, United States; Email: james.kincaid@marquette.edu

Emily E. Weinert — Department of Chemistry and Department of Biochemistry and Molecular Biology, The Pennsylvania State University, University Park, Pennsylvania 16802, United States; Ocid.org/0000-0002-4986-8682; Email: emily.weinert@psu.edu

Authors

Dayna C. Patterson – Department of Chemistry, The Pennsylvania State University, University Park, Pennsylvania 16802, United States; orcid.org/0000-0003-1950-0331

Yilin Liu – Department of Chemistry, Marquette University, Milwaukee, Wisconsin 53233, United States

Sayan Das – Department of Biochemistry and Molecular Biology, The Pennsylvania State University, University Park, Pennsylvania 16802, United States

Neela H. Yennawar — The Huck Institutes of the Life Sciences, The Pennsylvania State University, University Park, Pennsylvania 16802, United States; orcid.org/0000-0001-7278-659X

Jean-Paul Armache — Department of Biochemistry and Molecular Biology, The Pennsylvania State University, University Park, Pennsylvania 16802, United States

Complete contact information is available at: https://pubs.acs.org/10.1021/acs.biochem.1c00581

Notes

The authors declare no competing financial interest. DcpG: H3SIC7 9BACL

ACKNOWLEDGMENTS

This work was supported by NSF CHE1352040 (E.E.W.), Frasch Foundation Grant 824-H17 (E.E.W.), and NSF CHE200335 (E.E.W.) and NSF CHE2003345 (J.R.K.). D.C.P. is funded by a National Science Foundation Graduate Research Fellowship (1745025). We thank members of the Weinert lab for assistance and helpful suggestions. J.R.K. thanks Marquette University for partial support of Y.L. during this work. This work is based upon research conducted at the Cornell High Energy Synchrotron Source (CHESS), which is supported by the National Science Foundation and the National Institutes of Health/National Institute of General Medical Sciences under NSF award DMR-1829070 using the Macromolecular Diffraction at CHESS (MacCHESS) facility, which is supported by award GM-124166 from the National Institutes of Health, through its National Institute of General Medical Sciences.

REFERENCES

(1) Ravikanth, M.; Chandrashekar, T. K. (1995) Nonplanar porphyrins and their biological relevance: Ground and excited state dynamics. In *Coordination Chemistry*; Springer: Berlin, Heidelberg, pp. 105–188, DOI: 10.1007/BFb0036827.

- (2) Olea, C., Jr.; Boon, E. M.; Pellicena, P.; Kuriyan, J.; Marletta, M. A. Probing the Function of Heme Distortion in the H-NOX Family. *ACS Chem. Biol.* **2008**, *3*, 703–710.
- (3) Dutton, P. L.; Wilson, D. F.; Lee, C.-P. Oxidation-reduction potentials of cytochromes in mitochondria. *Biochemistry* **1970**, *9*, 5077–5082.
- (4) Blair, D. F.; Ellis, W. R., Jr.; Wang, H.; Gray, H. B.; Chan, S. I. Spectroelectrochemical study of cytochrome c oxidase: pH and temperature dependences of the cytochrome potentials. Characterization of site-site interactions. *J. Biol. Chem.* **1986**, *261*, 11524–11537.
- (5) Ayala, M. (2010) Redox Potential of Peroxidases. In *Biocatalysis Based on Heme Peroxidases: Peroxidases as Potential Industrial Biocatalysts*; (Torres, E.; Ayala, M., Eds.; pp. 61–77, Springer: Berlin, Heidelberg.
- (6) Battistuzzi, G.; Bellei, M.; Bortolotti, C. A.; Sola, M. Redox properties of heme peroxidases. *Arch. Biochem. Biophys.* **2010**, *500*, 21–36.
- (7) Tezcan, F. A.; Winkler, J. R.; Gray, H. B. Effects of Ligation and Folding on Reduction Potentials of Heme Proteins. *J. Am. Chem. Soc.* **1998**, *120*, 13383–13388.
- (8) Kassner, R. J. Effects of Nonpolar Environments on the Redox Potentials of Heme Complexes. *Proc. Natl. Acad. Sci. U. S. A.* **1972**, *69*, 2263–2267.
- (9) Mauk, A. G.; Moore, G. R. Control of metalloprotein redox potentials: what does site-directed mutagenesis of hemoproteins tell us? *IBIC, J. Biol. Inorg. Chem.* **1997**, *2*, 119–125.
- (10) Olea, C., Jr.; Kuriyan, J.; Marletta, M. A. Modulating Heme Redox Potential through Protein-Induced Porphyrin Distortion. *J. Am. Chem. Soc.* **2010**, *132*, 12794–12795.
- (11) Kitanishi, K.; Kobayashi, K.; Kawamura, Y.; Ishigami, I.; Ogura, T.; Nakajima, K.; Igarashi, J.; Tanaka, A.; Shimizu, T. Important Roles of Tyr43 at the Putative Heme Distal Side in the Oxygen Recognition and Stability of the Fe(II)—O2 Complex of YddV, a Globin-Coupled Heme-Based Oxygen Sensor Diguanylate Cyclase. *Biochemistry* **2010**, *49*, 10381–10393.
- (12) Sasakura, Y.; Hirata, S.; Sugiyama, S.; Suzuki, S.; Taguchi, S.; Watanabe, M.; Matsui, T.; Sagami, I.; Shimizu, T. Characterization of a Direct Oxygen Sensor Heme Protein fromEscherichia coli: EFFECTS OF THE HEME REDOX STATES AND MUTATIONS AT THE HEME-BINDING SITE ON CATALYSIS AND STRUCTURE. J. Biol. Chem. 2002, 277, 23821–23827.
- (13) Barreto, G. A.; Carepo, M. S. P.; Gondim, A. C. S.; Guimarães, W. G.; Lopes, L. G. F.; Bernhardt, P. V.; Paulo, T. F.; Sousa, E. H. S.; Diógenes, I. C. N. A spectroelectrochemical investigation of the heme-based sensor DevS from Mycobacterium tuberculosis: a redox versus oxygen sensor. FEBS J. 2019, 286, 4278–4293.
- (14) Honorio-Felício, N.; Carepo, M. S. P.; Paulo, T. D. F.; de França Lopes, L. G.; Sousa, E. H. S.; Diógenes, I. C. N.; Bernhardt, P. V. The Heme-Based Oxygen Sensor Rhizobium etli FixL: Influence of Auxiliary Ligands on Heme Redox Potential and Implications on the Enzyme Activity. *J. Inorg. Biochem.* **2016**, *164*, 34–41.
- (15) Shimizu, T.; Huang, D.; Yan, F.; Stranava, M.; Bartosova, M.; Fojtíková, V.; Martínková, M. Gaseous O2, NO, and CO in Signal Transduction: Structure and Function Relationships of Heme-Based Gas Sensors and Heme-Redox Sensors. *Chem. Rev.* **2015**, *115*, 6491–6533
- (16) Martínková, M.; Kitanishi, K.; Shimizu, T. Heme-based Globin-coupled Oxygen Sensors: Linking Oxygen Binding to Functional Regulation of Diguanylate Cyclase, Histidine Kinase, and Methylaccepting Chemotaxis. *J. Biol. Chem.* **2013**, 288, 27702–27711.
- (17) Walker, J. A.; Rivera, S.; Weinert, E. E. (2017) Mechanism and Role of Globin-Coupled Sensor Signalling. In *Adv Microb Physiol*; Poole, R. K., Ed.; pp. 133–169, Academic Press, DOI: 10.1016/bs.ampbs.2017.05.003.
- (18) Jia, X.; Wang, J.-B.; Rivera, S.; Duong, D.; Weinert, E. E. An O2-Sensing Stressosome from a Gram Negative Bacterium. *Nat. Commun.* **2016**, *7*, 12381.

- (19) Ma, X.; Sayed, N.; Beuve, A.; van den Akker, F. NO and CO differentially activate soluble guanylyl cyclase via a heme pivot-bend mechanism. *EMBO J.* **2007**, *26*, 578–588.
- (20) Burns, J. L.; Deer, D. D.; Weinert, E. E. Oligomeric state affects oxygen dissociation and diguanylate cyclase activity of globin coupled sensors. *Mol. BioSyst.* **2014**, *10*, 2823–2826.
- (21) Patterson, D. C.; Ruiz, M. P.; Yoon, H.; Walker, J. A.; Armache, J.-P.; Yennawar, N. H.; Weinert, E. E. Differential ligand-selective control of opposing enzymatic activities within a bifunctional c-di-GMP enzyme. *Proc. Natl. Acad. Sci.* **2021**, *118*, No. e2100657118.
- (22) Hengge, R. Principles of c-di-GMP signalling in bacteria. *Nat. Rev. Microbiol.* **2009**, *7*, 263–273.
- (23) Suter-Crazzolara, C.; Unsicker, K. Improved expression of toxic proteins in E.coli. *Biotechniques* 1995, 19, 202–204.
- (24) Boon, E. M.; Huang, S. H.; Marletta, M. A. A molecular basis for NO selectivity in soluble guanylate cyclase. *Nat. Chem. Biol.* **2005**, 1, 53–59.
- (25) Karow, D. S.; Pan, D.; Tran, R.; Pellicena, P.; Presley, A.; Mathies, R. A.; Marletta, M. A. Spectroscopic Characterization of the Soluble Guanylate Cyclase-like Heme Domains from Vibrio cholerae and Thermoanaerobacter tengcongensis. *Biochemistry* **2004**, *43*, 10203–10211.
- (26) Weinert, E. E.; Plate, L.; Whited, C. A.; Olea, C., Jr.; Marletta, M. A. Determinants of ligand affinity and heme reactivity in H-NOX domains. *Angew. Chem., Int. Ed.* **2010**, *49*, 720–723.
- (27) Ishitsuka, Y.; Araki, Y.; Tanaka, A.; Igarashi, J.; Ito, O.; Shimizu, T. Arg97 at the heme-distal side of the isolated heme-bound PAS domain of a heme-based oxygen sensor from Escherichia coli (Ec DOS) plays critical roles in autoxidation and binding to gases, particularly O2. *Biochemistry* **2008**, *47*, 8874–8884.
- (28) Burns, J. L.; Rivera, S.; Deer, D. D.; Joynt, S. C.; Dvorak, D.; Weinert, E. E. Oxygen and c-di-GMP Binding Control Oligomerization State Equilibria of Diguanylate Cyclase-Containing Globin Coupled Sensors. *Biochemistry* **2016**, *55*, 6642–6651.
- (29) Hopkins, J. B.; Gillilan, R. E.; Skou, S. BioXTAS RAW: improvements to a free open-source program for small-angle X-ray scattering data reduction and analysis. *J. Appl. Crystallogr.* **2017**, *50*, 1545–1553.
- (30) Franke, D.; Petoukhov, M. V.; Konarev, P. V.; Panjkovich, A.; Tuukkanen, A.; Mertens, H. D. T.; Kikhney, A. G.; Hajizadeh, N. R.; Franklin, J. M.; Jeffries, C. M.; Svergun, D. I. ATSAS 2.8: a comprehensive data analysis suite for small-angle scattering from macromolecular solutions. *J. Appl. Crystallogr.* **2017**, *50*, 1212–1225.
- (31) Svergun, D. I. Determination of the regularization parameter in indirect-transform methods using perceptual criteria. *J. Appl. Crystallogr.* **1992**, 25, 495–503.
- (32) Svergun, D. I. Restoring Low Resolution Structure of Biological Macromolecules from Solution Scattering Using Simulated Annealing. *Biophys. J.* **1999**, *76*, 2879–2886.
- (33) Volkov, V. V.; Svergun, D. I. Uniqueness of ab initio shape determination in small-angle scattering. *J. Appl. Crystallogr.* **2003**, *36*, 860–864.
- (34) Svergun, D.; Barberato, C.; Koch, M. H. J. CRYSOL a Program to Evaluate X-ray Solution Scattering of Biological Macromolecules from Atomic Coordinates. *J. Appl. Crystallogr.* **1995**, 28, 768–773.
- (35) Yang, J.; Yan, R.; Roy, A.; Xu, D.; Poisson, J.; Zhang, Y. The I-TASSER Suite: protein structure and function prediction. *Nat. Methods* **2015**, *12*, 7–8.
- (36) The PyMOL Molecular Graphics System, Version 1.2r3pre, Schrödinger, LLC.
- (37) Pettersen, E. F.; Goddard, T. D.; Huang, C. C.; Couch, G. S.; Greenblatt, D. M.; Meng, E. C.; Ferrin, T. E. UCSF Chimera–A visualization system for exploratory research and analysis. *J. Comput. Chem.* **2004**, *25*, 1605–1612.
- (38) Panjkovich, A.; Svergun, D. I. Deciphering conformational transitions of proteins by small angle X-ray scattering and normal mode analysis. *Phys. Chem. Chem. Phys.* **2016**, *18*, 5707–5719.

- (39) Kastner, B.; Fischer, N.; Golas, M. M.; Sander, B.; Dube, P.; Boehringer, D.; Hartmuth, K.; Deckert, J.; Hauer, F.; Wolf, E.; Uchtenhagen, H.; Urlaub, H.; Herzog, F.; Peters, J. M.; Poerschke, D.; Lührmann, R.; Stark, H. GraFix: sample preparation for single-particle electron cryomicroscopy. *Nat. Methods* **2008**, *5*, 53–55.
- (40) Stark, H. GraFix: stabilization of fragile macromolecular complexes for single particle cryo-EM. *Methods Enzymol.* **2010**, *481*, 109–126
- (41) Tang, G.; Peng, L.; Baldwin, P. R.; Mann, D. S.; Jiang, W.; Rees, I.; Ludtke, S. J. EMAN2: An extensible image processing suite for electron microscopy. *J. Struct. Biol.* **2007**, *157*, 38–46.
- (42) Punjani, A.; Rubinstein, J. L.; Fleet, D. J.; Brubaker, M. A. cryoSPARC: algorithms for rapid unsupervised cryo-EM structure determination. *Nat. Methods* **2017**, *14*, 290–296.
- (43) Zhang, W.; Olson, J. S.; Phillips, G. N., Jr. Biophysical and kinetic characterization of HemAT, an aerotaxis receptor from Bacillus subtilis. *Biophys. J.* **2005**, *88*, 2801–2814.
- (44) Kelley, L. A.; Mezulis, S.; Yates, C. M.; Wass, M. N.; Sternberg, M. J. E. The Phyre2 web portal for protein modeling, prediction and analysis. *Nat. Protoc.* **2015**, *10*, 845.
- (45) Weinert, E. E.; Phillips-Piro, C. M.; Marletta, M. A. Porphyrin π -stacking in a heme protein scaffold tunes gas ligand affinity. *J. Inorg. Biochem.* **2013**, *127*, 7–12.
- (46) Hargrove, M. S.; Wilkinson, A. J.; Olson, J. S. Structural Factors Governing Hemin Dissociation from Metmyoglobin. *Biochemistry* **1996**, *35*, 11300–11309.
- (47) Rivera, S.; Young, P. G.; Hoffer, E. D.; Vansuch, G. E.; Metzler, C. L.; Dunham, C. M.; Weinert, E. E. Structural Insights into Oxygen-Dependent Signal Transduction within Globin Coupled Sensors. *Inorg. Chem.* **2018**, *57*, 14386–14395.
- (48) Bennett, B. D.; Kimball, E. H.; Gao, M.; Osterhout, R.; Van Dien, S. J.; Rabinowitz, J. D. Absolute metabolite concentrations and implied enzyme active site occupancy in Escherichia coli. *Nat. Chem. Biol.* **2009**, *5*, 593–599.
- (49) Uchida, T.; Kitagawa, T. Mechanism for transduction of the ligand-binding signal in heme-based gas sensory proteins revealed by resonance Raman spectroscopy. *Acc. Chem. Res.* **2005**, *38*, *662*–*670*.
- (50) El-Mashtoly, S. F.; Kitagawa, T. Structural chemistry involved in information detection and transmission by gas sensor heme proteins: Resonance Raman investigation. *Pure Appl. Chem.* **2008**, *80*, 2667–2678.
- (51) Schweitzer-Stenner, R. Using spectroscopic tools to probe porphyrin deformation and porphyrin-protein interactions. *J. Porphyrins Phthalocyanines* **2011**, *15*, 312–337.
- (52) Tran, R.; Boon, E. M.; Marletta, M. A.; Mathies, R. A. Resonance Raman Spectra of an O2-Binding H-NOX Domain Reveal Heme Relaxation upon Mutation. *Biochemistry* **2009**, *48*, 8568–8577.
- (53) Sawai, H.; Yoshioka, S.; Uchida, T.; Hyodo, M.; Hayakawa, Y.; Ishimori, K.; Aono, S. Molecular oxygen regulates the enzymatic activity of a heme-containing diguanylate cyclase (HemDGC) for the synthesis of cyclic di-GMP. *Biochim. Biophys. Acta, Proteins Proteomics* **2010**, *1804*, 166–172.
- (54) El-Mashtoly, S. F.; Gu, Y.; Yoshimura, H.; Yoshioka, S.; Aono, S.; Kitagawa, T. Protein conformation changes of HemAT-Bs upon ligand binding probed by ultraviolet resonance Raman spectroscopy. *J. Biol. Chem.* **2008**, 283, 6942–6949.
- (55) Varadarajan, R.; Zewert, T. E.; Gray, H. B.; Boxer, S. G. Effects of buried ionizable amino acids on the reduction potential of recombinant myoglobin. *Science* **1989**, *243*, 69–72.
- (56) Gunner, M. R.; Honig, B. Electrostatic control of midpoint potentials in the cytochrome subunit of the Rhodopseudomonas viridis reaction center. *Proc. Natl. Acad. Sci. U. S. A.* **1991**, *88*, 9151–9155.
- (57) Shelnutt, J. A.; Song, X.-Z.; Ma, J.-G.; Jia, S.-L.; Jentzen, W.; Medforth, C. J. Nonplanar porphyrins and their significance in proteins. *Chem. Soc. Rev.* **1998**, *27*, 31.
- (58) Ma, J. G.; Vanderkooi, J. M.; Zhang, J.; Jia, S. L.; Shelnutt, J. A. Resonance Raman investigation of nickel microperoxidase-11. *Biochemistry* **1999**, *38*, 2787–2795.

- (59) Chen, Z.; Ost, T. W. B.; Schelvis, J. P. M. Phe393 Mutants of Cytochrome P450 BM3 with Modified Heme Redox Potentials Have Altered Heme Vinyl and Propionate Conformations. *Biochemistry* **2004**, *43*, 1798–1808.
- (60) Lee, K. B.; Jun, E.; La Mar, G. N.; Rezzano, I. N.; Pandey, R. K.; Smith, K. M.; Walker, F. A.; Buttlaire, D. H. Influence of heme vinyl- and carboxylate-protein contacts on structure and redox properties of bovine cytochrome b5. *J. Am. Chem. Soc.* **1991**, *113*, 3576–3583.
- (61) Reid, L. S.; Lim, A. R.; Mauk, A. G. Role of heme vinyl groups in cytochrome b5 electron transfer. *J. Am. Chem. Soc.* **1986**, *108*, 8197–8201.
- (62) Das, D. K.; Medhi, O. K. The role of heme propionate in controlling the redox potential of heme: Square wave voltammetry of protoporphyrinato IX iron(III) in aqueous surfactant micelles. *J. Inorg. Biochem.* **1998**, *70*, 83–90.
- (63) Huang, Q.; Schweitzer-Stenner, R. Non-planar heme deformations and excited state displacements in horseradish peroxidase detected by Raman spectroscopy at Soret excitation. *J. Raman Spectrosc.* **2005**, *36*, 363–375.
- (64) Rwere, F.; Mak, P. J.; Kincaid, J. R. Resonance Raman determination of vinyl group disposition in different derivatives of native myoglobin and its heme-disoriented form. *J. Raman Spectrosc.* **2014**, *45*, 97–104.
- (65) Rwere, F.; Mak, P. J.; Kincaid, J. R. The impact of altered protein-heme interactions on the resonance Raman spectra of heme proteins. *Studies of heme rotational disorder*. *Biopolymers* **2008**, 89, 179–186.
- (66) Milazzo, L.; Exertier, C.; Becucci, M.; Freda, I.; Montemiglio, L. C.; Savino, C.; Vallone, B.; Smulevich, G. Lack of orientation selectivity of the heme insertion in murine neuroglobin revealed by resonance Raman spectroscopy. *FEBS J.* **2020**, *287*, 4082–4097.
- (67) Cerda-Colón, J. F.; Silfa, E.; López-Garriga, J. Unusual Rocking Freedom of the Heme in the Hydrogen Sulfide-Binding Hemoglobin from *Lucina pectinata*. *J. Am. Chem. Soc.* **1998**, *120*, 9312–9317.
- (68) Peterson, E. S.; Friedman, J. M.; Chien, E. Y. T.; Sligar, S. G. Functional implications of the proximal hydrogen-bonding network in myoglobin: A resonance Raman and kinetic study of Leu89, Ser92, His97, and F-helix swap mutants. *Biochemistry* **1998**, *37*, 12301–12319.
- (69) Funk, W. D.; Lo, T. P.; Mauk, M. R.; Brayer, G. D.; MacGillivray, R. T. A.; Mauk, A. G. Mutagenic, electrochemical, and crystallographic investigation of the cytochrome b5 oxidation-reduction equilibrium: involvement of asparagine-57, serine-64, and heme propionate-7. *Biochemistry* **1990**, *29*, 5500–5508.
- (70) Bock, C. W.; Trachtman, M.; George, P. A Molecular orbital study of the rotation about the C—C bond in styrene. *Chem. Phys.* **1985**, *93*, 431–443.
- (71) Satterlee, J. D.; Erman, J. E. Temperature and pH dependence of the proton magnetic hyperfine resonances of cytochrome c peroxidase-cyanide, Evidence for hindered vinyl group rotation as a mediator of the enzymes activity. *J. Biol. Chem.* **1983**, 258, 1050–1056
- (72) Mak, P. J.; Denisov, I. G.; Grinkova, Y. V.; Sligar, S. G.; Kincaid, J. R. Defining CYP3A4 Structural Responses to Substrate Binding. Raman Spectroscopic Studies of a Nanodisc-Incorporated Mammalian Cytochrome P450. *J. Am. Chem. Soc.* **2011**, *133*, 1357–1366.
- (73) Hu, S.; Smith, K. M.; Spiro, T. G. Assignment of Protoheme Resonance Raman Spectrum by Heme Labeling in Myoglobin. *J. Am. Chem. Soc.* **1996**, *118*, 12638–12646.
- (74) Deinum, G.; Stone, J. R.; Babcock, G. T.; Marletta, M. A. Binding of nitric oxide and carbon monoxide to soluble guanylate cyclase as observed with resonance Raman spectroscopy. *Biochemistry* **1996**, 35, 1540–1547.
- (75) Aono, S.; Kato, T.; Matsuki, M.; Nakajima, H.; Ohta, T.; Uchida, T.; Kitagawa, T. Resonance Raman and ligand binding studies of the oxygen-sensing signal transducer protein HemAT from Bacillus subtilis. J. Biol. Chem. 2002, 277, 13528–13538.

- (76) Mak, P. J.; Thammawichai, W.; Wiedenhoeft, D.; Kincaid, J. R. Resonance Raman Spectroscopy Reveals pH-Dependent Active Site Structural Changes of Lactoperoxidase Compound 0 and Its Ferryl Heme O-O Bond Cleavage Products. J. Am. Chem. Soc. 2015, 137, 349–361.
- (77) Tamura, K.; Nakamura, H.; Tanaka, Y.; Oue, S.; Tsukamoto, K.; Nomura, M.; Tsuchiya, T.; Adachi, S.; Takahashi, S.; Iizuka, T.; Shiro, Y. Nature of endogenous ligand binding to heme iron in oxygen sensor FixL. *J. Am. Chem. Soc.* **1996**, *118*, 9434–9435.
- (78) Brogioni, S.; Stampler, J.; Furtmüller, P. G.; Feis, A.; Obinger, C.; Smulevich, G. The role of the sulfonium linkage in the stabilization of the ferrous form of myeloperoxidase: A comparison with lactoperoxidase. *Biochim. Biophys. Acta, Proteins Proteomics* **2008**, 1784, 843–849.
- (79) Capece, L.; Marti, M. A.; Crespo, A.; Doctorovich, F.; Estrin, D. A. Heme protein oxygen affinity regulation exerted by proximal effects. J. Am. Chem. Soc. 2006, 128, 12455–12461.
- (80) Jentzen, W.; Simpson, M. C.; Hobbs, J. D.; Song, X.; Ema, T.; Nelson, N. Y.; Medforth, C. J.; Smith, K. M.; Veyrat, M.; Mazzanti, M.; Ramasseul, R.; Marchon, J.-C.; Takeuchi, T.; Goddard, W. A., III; Shelnutt, J. A. Ruffling in a Series of Nickel(II) meso-Tetrasubstituted Porphyrins as a Model for the Conserved Ruffling of the Heme of Cytochromes c. J. Am. Chem. Soc. 1995, 117, 11085–11097.
- (81) Jentzen, W.; Song, X.-Z.; Shelnutt, J. A. Structural Characterization of Synthetic and Protein-Bound Porphyrins in Terms of the Lowest-Frequency Normal Coordinates of the Macrocycle. *J. Phys. Chem. B* 1997, 101, 1684–1699.